International Journal of Fluid Power, 2015
Vol. 16, No. 1, 35–51, http://dx.doi.org/10.1080/14399776.2015.1016839

Taylor & Francis
Taylor & Francis Group

Port and case flow temperature prediction for axial piston machines

L. Shang* and M. Ivantysynova

Department of Agricultural and Biological Engineering, Purdue University, 225 South University Street, West Lafayette, IN 47907-2938, USA

(*Received 22 August 2014; accepted 5 February 2015*)

Researchers at Purdue's Maha Fluid Power Research Center have developed models that will enable computational design of piston machines. The core of the in-house developed program forms multi-domain models capturing the fluid–structure interaction phenomena taking place in the main lubricating interfaces (piston/cylinder, cylinder block/valve plate, and slipper/swash plate) of axial piston machines. The model allows studying the influence of a given pump or motor design on machine performance, power loss, and energy dissipation in those main lubricating interfaces. The behavior of the fluid film in these lubricating interfaces as well as the shape of the solid parts is temperature and pressure dependent. In order to solve for non-isothermal flow and to consider elasto-hydrodynamic effects, port and case temperatures are needed as boundary condition for the model. In case of analysis and optimization of existing pumps and motors, those boundary conditions can be taken from steady-state measurements; however, when using the model to design a new unit, this information is not available. The temperature prediction model proposed in this paper fills this gap. The model can predict the outlet and case temperature for a chosen inlet temperature based on known fluid properties and calculated energy dissipation in the rotating group of an axial piston pump. The model also considers the temperature change due to fluid compression/expansion and estimated churning losses for a given axial piston machine.

Keywords: axial piston machines; lubrication; computational pump design; thermodynamic model; heat-transfer model; outlet temperature; case temperature

1. Introduction

After decades of research on studying the fluid film behavior in the main tribological interfaces of axial piston machines, the authors' research team proposed a fluid–structure and thermal interaction model (FSTI) for the three main lubricating interfaces of swash plate-type axial piston machine (piston/cylinder, slipper/swash plate, and cylinder block/valve plate interfaces), details can be found in Pelosi and Ivantysynova (2012, 2013), Zecchi and Ivantysynova (2013) and Schenk and Ivantysynova (2014). The FSTI model allows predicting fluid film behavior in three lubricating interfaces based on non-isothermal flow conditions, and macro- and micro-motion of parts as well as surface deformation due to pressure and thermal loading.

In order to solve for non-isothermal flow in lubricating interfaces and to consider surface deformation due to thermal loading, a detailed heat-transfer model of the entire axial piston machine is included in the FSTI model (Pelosi 2012; Zecchi 2013). The three-dimensional (3D) heat-transfer model included in FSTI requires boundary temperatures to be solved numerically. These boundary conditions are inlet port temperature, outlet port temperature, and case flow temperature.

When the FSTI model is used to analyze or optimize an existing pump or motor, the required boundary temperatures can be taken from steady-state measurement conducted on the pump or motor of interest.

However, the FSTI model can also be used to support the design of new pumps and motors. At this point, measurement data are not available. Therefore, the authors' research team started the development of a port and case flow temperature prediction model few years ago. A flow temperature prediction model was proposed by Grönberg (2011). This model was further developed by Zecchi *et al.* (2013) A drawback of this model is its sensitivity to the user's inputs, especially to the heat-transfer area and the heat-transfer coefficients. A slightly inaccurate user's inputs will lead to a large error in the case flow and port flow temperature prediction. As a consequence, the FSTI model will predict very different fluid film behaviors for different given combinations of inlet, outlet, and case flow temperature. In real world, there is only one true combination of these temperatures for a given pump design, given fluid, and given operating conditions. The authors conducted a simulation study with the FSTI model to investigate the sensitivity of these boundary temperatures on the fluid film behaviors in the three lubricating interfaces. Figure 1 shows a comparison of power loss and leakage obtained for the same pump design and same fluid when varying the outlet and case temperature. The power loss and leakage values are outputs of the FSTI simulation model. The FSTI simulations have been conducted for the same pump at same inlet temperature of the fluid. But outlet port temperature and case temperature were

*Corresponding author. Email: shangl@purdue.edu

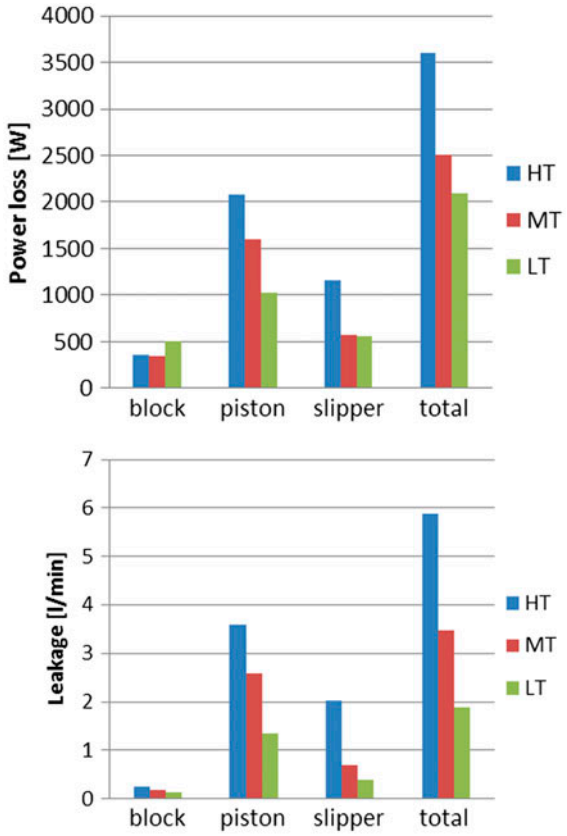

Figure 1. FSTI simulation results.

modified. Table 1 shows the inlet flow temperature, the outlet flow temperature, and the case flow temperature for these three simulations, labeled HT (higher temperature), MT (measured temperature), and LT (lower temperature).

The simulation results shown in Figure 1 demonstrate the significance of pump port and case flow temperature for a reliable prediction of fluid film behaviors in these important pump interfaces. The upper figure shows the power losses generated in the three lubricating interfaces and the sum of the three marked as 'total power loss.' An obvious reduction on power loss can be found with decreasing temperature. As can be seen from Figure 1, the outlet port and case temperatures have also a large impact on the predicted leakage. From this simulation study, it is obvious that the prediction of lubricating interfaces' behavior including energy dissipation due to viscous flow requires very good estimate of port and case flow temperatures.

Table 1. Input temperatures for three sets of simulations.

	HT	MT	LT
inlet temperature [°C]	52.4	52.4	52.4
outlet temperature [°C]	70	60.5	52.4
case temperature [°C]	100	79.4	52.4

For this reason, in this paper, the authors presented generic and in some way rather simplified thermodynamic pump model. The goal was to develop a model that calculates outlet port and case flow temperatures based on known fluid properties, inlet temperature, and estimated energy dissipation/power loss for a given pump design. In order to allow the use of the model for different pump and motors sizes, linear scaling laws, which are used for pump design by most of the pump and motor manufactures, are incorporated in the proposed port and case temperature prediction model. In order to estimate the energy dissipation in lubricating gaps, a co-simulation between the FSTI model and the case and temperature prediction model is required. The required procedure will be explained in the next chapter.

2. Pump port and case temperatures prediction model

It is known, since the work of Witt (1974), that the overall efficiency of hydrostatic pumps and motors can be determined with temperature and pressure measurement combination and an accurate description of the fluid properties. The determination of overall efficiency based on thermodynamics requires the determination of enthalpy difference between inlet and outlet. While Witt calculates pump loss from measured flow temperature and known fluid properties, the authors of this paper wish to determine port and case flow temperature from given loss of the pump or motor and known fluid properties.

For the presented model, the authors propose to divide the fluid volume of a pump or motor into four volumes as shown in Figure 2. The volumes are divided in case volume, displacement chamber volume, inlet port volume, and outlet port volume. The heat and mass transfer in an axial piston machine under steady-state condition is illustrated schematically in Figure 2. The inlet mass flow rate $\dot{m}_{\text{in}}$ enters the unit through the inlet port volume. Part of the inlet mass flow rate transfers through the displacement chamber volume to the outlet

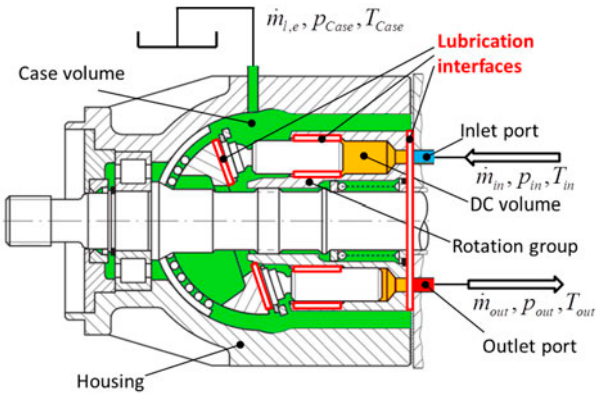

Figure 2. Definition of the control volumes.

port volume, and leaves the unit as the outlet mass flow rate $\dot{m}_{out}$, the remaining part of the inlet mass flow rate transfers through the displacement chamber volume to the case volume, and leaves the unit as external leakage mass flow rate $\dot{m}_{l,e}$. The internal leakage mass flow rate $\dot{m}_{l,i}$ transfers from the outlet port volume through the displacement volume into the inlet port volume. Due to the conservation of mass flow rate, the internal leakage mass flow rate is added to the mass flow rate from the inlet port to the displacement chamber, and the mass flow from the displacement chamber to the outlet port.

The heat-transfer in an axial piston machine running under steady-state condition is illustrated schematically in Figure 3. Three red arrows in the housing block represent the convective heat-transfer between the displacement volume and the solid parts, the case volume and the solid parts, and the case volume and the inner housing surface. The red arrow on the outside of the housing block represents the natural heat-transfer between the housing outer surface and the ambient air. The white arrow represents the radiation.

As it is shown in Figure 3, the internal leakage mass flow rate forms two closed loops between the inlet port volume, the displacement chamber volume, and the outlet port volume. The internal mass flow rate has limited impact on the pump flow temperature because of these two closed loops. Thus, in order to simplify the pump flow temperatures prediction model, the internal leakage mass flow rate is neglected. The inlet port volume and the outlet port volume are merged into the displacement chamber volume as shown in the Figure 4.

The convective heat-transfer between the case volume and the inner surface of the housing is neglected due to the small temperature difference. Also, radiation is neglected due to its limited impact on the port and case temperatures. All the simplifications mentioned above are shown in Figure 4.

Figure 4 shows that the pressure in and out of the displacement chamber volume changes from p_{in} to p_{out}, which contributes to the temperature variation due to compression or expansion, respectively. The convective

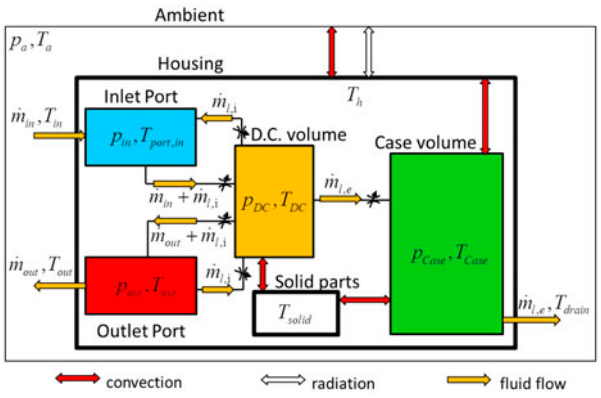

Figure 3. Schematic of the heat and mass transfer in the axial piston machine.

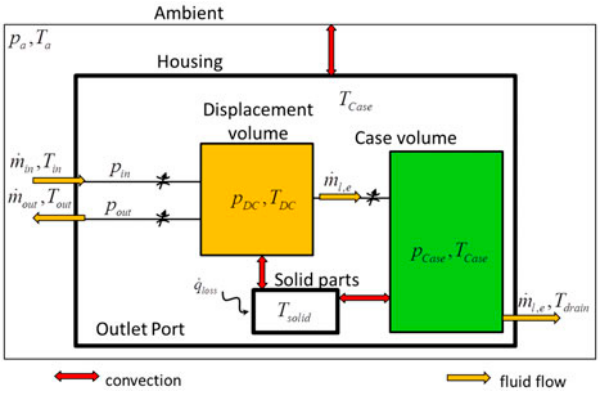

Figure 4. Simplified schematic of the heat and mass transfer in the axial piston machine.

heat-transfer between the solid parts and the displacement chamber volume contributes to the temperature variation as well. The red dashed line in Figure 5 connects the inlet and outlet state in the enthalpy–entropy diagram of the hydraulic fluid based on the measured pressure and temperature. Due to the heat-transfer, the real compression process does not follow a vertical line. Since in a real axial piston machine, the fluid pressure changes only over a very short time period and the heat-transfer occurs under constant pressure mostly, the real compression process has been divided into two vectors as shown in Figure 5. The vertical black vector represents an adiabatic compression, and the green vector represents the temperature variation due to the heat-transfer at constant pressure. This allows separate study on the temperature variation due to the pressure change and due to the heat-transfer.

The case temperature variation can also be divided into the adiabatic compression or expansion and the heat-transfer.

Therefore, the proposed pump outlet port and case flow temperatures prediction model includes two separated modules, the *thermodynamic* module, and the

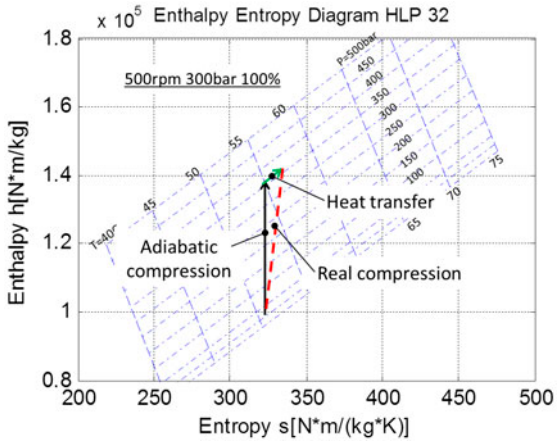

Figure 5. Compression process in the displacement chamber.

heat-transfer module, considering the temperature variation due to the pressure change.

2.1. Thermodynamic module

The thermodynamic module predicts the temperature variation due to the pressure changes assuming adiabatic compression and expansion. The enthalpy and entropy of the compressible fluid need to be solved as a necessary step.

The specific enthalpy and entropy of compressible fluid can be described as functions of temperature and pressure:

$$\begin{aligned} h &= h(T,\ p) \\ s &= s(T,\ p) \end{aligned} \tag{2.1}$$

The total differential of the enthalpy and the entropy can be written as:

$$\begin{aligned} \mathrm{d}h &= \left(\frac{\partial h}{\partial T}\right)_p \cdot \mathrm{d}T + \left(\frac{\partial h}{\partial p}\right)_T \cdot \mathrm{d}p \\ \mathrm{d}s &= \left(\frac{\partial s}{\partial T}\right)_p \cdot \mathrm{d}T + \left(\frac{\partial s}{\partial p}\right)_T \cdot \mathrm{d}p \end{aligned} \tag{2.2}$$

The derivations of the caloric constitutive equations yield:

$$c_p = \left(\frac{\partial h}{\partial T}\right)_p \tag{2.3}$$

Using the Maxwell relation:

$$\mathrm{d}s = \left(\frac{\partial s}{\partial T}\right)_p \cdot \mathrm{d}T - \left(\frac{\partial v}{\partial T}\right)_p \cdot \mathrm{d}p \tag{2.4}$$

where v is the specific volume of the fluid and substituting $\mathrm{d}h$ and $\mathrm{d}s$ into $\mathrm{d}s = T \cdot \mathrm{d}s + v \cdot \mathrm{d}p$

we obtain:

$$\left[\left(\frac{\partial h}{\partial p}\right)_T + T\left(\frac{\partial v}{\partial T}\right)_p - v\right]\mathrm{d}p = \left[T\left(\frac{\partial s}{\partial T}\right)_p - \left(\frac{\partial h}{\partial T}\right)_p\right]\mathrm{d}T \tag{2.5}$$

At constant temperature:

$$\begin{aligned} \left[\left(\frac{\partial h}{\partial p}\right)_T + T\left(\frac{\partial v}{\partial T}\right)_p - v\right]\mathrm{d}p &= 0 \\ \left(\frac{\partial h}{\partial p}\right)_T &= v - T\left(\frac{\partial v}{\partial T}\right)_p \end{aligned} \tag{2.6}$$

At constant pressure:

$$\begin{aligned} 0 &= \left[T\left(\frac{\partial s}{\partial T}\right)_p - \left(\frac{\partial h}{\partial T}\right)_p\right]\mathrm{d}T \\ \left(\frac{\partial s}{\partial T}\right)_p &= \frac{1}{T}\left(\frac{\partial h}{\partial T}\right)_p = \frac{1}{T}c_p \end{aligned} \tag{2.7}$$

Combining Equations (2.3) and (2.6) and substituting into Equation (2.2), we obtain:

$$\mathrm{d}h = c_p \cdot \mathrm{d}T + \left(v - T \cdot \left(\frac{\partial v}{\partial T}\right)_p\right) \cdot \mathrm{d}p \tag{2.8}$$

Substituting Equation (2.7) into Equation (2.4) gives:

$$\mathrm{d}s = c_p \cdot \frac{\mathrm{d}T}{T} - \left(\frac{\partial v}{\partial T}\right)_p \cdot \mathrm{d}p \tag{2.9}$$

Integrating Equations (2.8) and (2.9) at T_o and p_o yields:

$$\begin{aligned} h &= h_o(T_o) + \int_{T_o}^{T} c_p \cdot \mathrm{d}T + \int_{p_0}^{p} v \cdot \mathrm{d}p - \int_{p_0}^{p} T \cdot \left(\frac{\partial v}{\partial T}\right)_p \cdot \mathrm{d}p \\ s &= s_o(T_o) + \int_{T_o}^{T} \frac{c_p}{T} \cdot \mathrm{d}T - \int_{p_0}^{p} \left(\frac{\partial v}{\partial T}\right)_p \cdot \mathrm{d}p \end{aligned} \tag{2.10}$$

Based on the adiabatic compression assumption, the entropy of the fluid before and after the compression or the expansion is the same:

$$\begin{aligned} s_1 &= s_2 \\ \int_{T_o}^{T_1} \frac{c_p}{T} \cdot \mathrm{d}T - \int_{p_0}^{p_1} \left(\frac{\partial v}{\partial T}\right)_p \cdot \mathrm{d}p &= \int_{T_o}^{T_2} \frac{c_p}{T} \cdot \mathrm{d}T - \int_{p_0}^{p_2} \left(\frac{\partial v}{\partial T}\right)_p \cdot \mathrm{d}p \end{aligned} \tag{2.11}$$

The temperature of the fluid after the adiabatic compression or expansion in both displacement and case volume, $T_{\text{adia\_DC}}$ and $T_{\text{adia\_Case}}$, can be solved using Equation (2.11).

Figure 6 shows the enthalpy–entropy diagram of the HLP-32 which was calculated from the thermodynamic module. The enthalpy–entropy diagram in Figure 6 for HLP-32 shows very comparable values to the published data by Oppermann (2006).

2.2. Heat-transfer module

The heat-transfer module corrects the result of thermodynamic module using heat-transfer calculation.

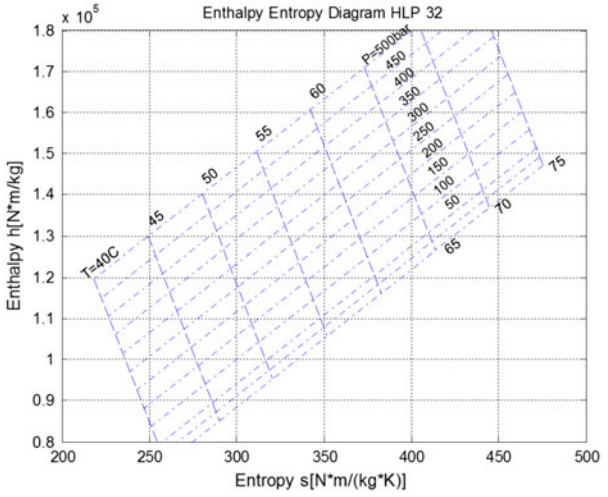

Figure 6. Enthalpy–entropy diagram of HLP-32 calculated from the thermodynamic module.

The heat-transfer module, which forms a part of the model presented in this paper, is based on a large experimental study involving different axial piston designs and pump/motor sizes, and it represents a rather empirical model. The main source of power loss in axial piston machines is the three lubricating interfaces. When studying the behavior of these lubricating interfaces, it can be shown that the energy dissipation in the lubricating film is not evenly distributed. Eccentric loading of the surfaces together with surface deformation due to pressure and thermal loads leads to usually rather small areas of very small film thickness with very high shearing and locally very high energy dissipation. The heat generated in those small areas of the lubricating gaps transfers into case volume and outlet port through a rather complex heat-transfer combining convection and conduction. Because of the very small film thickness in those small areas, the convection effect is limited through the limited leakage flow.

Also, a study of temperature distribution in the solid parts forming the lubricating interfaces was conducted by Zecchi (2013). This study shows that the temperatures in the solid parts are locally higher than both the case flow temperature (sometimes in order of 20 °C) and outlet flow temperature (sometimes in order of 50 °C), which indicates that a good amount of heat is transferred from the solid parts into both the case and displacement chamber. Temperature distribution measurements conducted on the rotating cylinder block of a stock swash plate axial piston machine by Olems (2001) showed also areas of locally higher temperatures than the oil in the displacement chamber and pump case.

Based on these observations from conducted measurements on stock axial piston machines, the following simplified assumption was introduced in the heat-transfer model shown in Figure 7. The rate of heat flow $\dot{q}_{\text{loss}}$ generated by the pump power loss is assumed to be transferred through conduction into the solid parts and from the solid parts into both the displacement chamber volume and the case volume at the same time.

The simplified three volume model is shown in Figure 7, where $\dot{q}_{\text{loss}}$ represents the total power loss of the pump, $\dot{q}_{s\_\text{DC}}$ and $\dot{q}_{s\_\text{Case}}$ represent the rate of heat flow from the solid parts into the displacement chamber volume and the case volume, respectively. According to

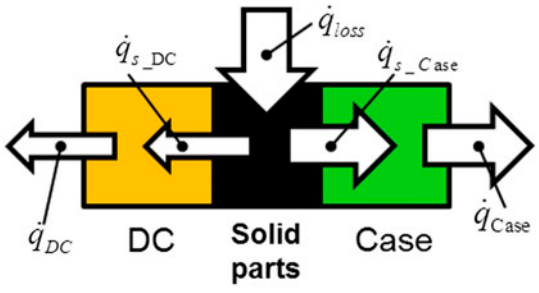

Figure 7. Three volumes heat-transfer model.

the equilibrium of rate of heat flow in the volume of the solid parts, we can write:

$$\dot{q}_{\text{loss}} = \dot{q}_{s\_\text{DC}} + \dot{q}_{s\_\text{Case}} \tag{2.12}$$

According to the equilibrium of rate of heat flow in the displacement chamber volume, we obtain:

$$\dot{q}_{\text{DC}} = \dot{q}_{s\_\text{DC}} \tag{2.13}$$

Finally, the equilibrium of rate of heat flow in the case volume yields::

$$\dot{q}_{\text{Case}} = \dot{q}_{s\_\text{Case}} \tag{2.14}$$

The rate of heat flow leaving the displacement chamber with the outlet flow rate is calculated from the outlet mass flow rate, the temperature differential, and the fluid specific heat capacity:

$$\dot{q}_{\text{DC}} = \dot{m}_{\text{out}} \cdot \int_{T_{\text{adia\_DC}}}^{T_{\text{out}}} c_p \mathrm{d}T \tag{2.15}$$

where $T_{\text{adia\_DC}}$ is the fluid temperature after adiabatic compression or expansion in the displacement chamber volume calculated in the thermodynamic module.

The rate of heat flow leaving the case volume with the case flow rate and due to the natural heat-transfer flow into the air is calculated from the case mass flow rate, temperature differential, fluid specific heat capacity, the air temperature, and the overall natural heat-transfer coefficient of the pump outer housing surface:

$$\dot{q}_{\text{Case}} = \dot{m}_{\text{Case}} \cdot \int_{T_{\text{adia\_Case}}}^{T_{\text{Case}}} c_p \mathrm{d}T + k_{\text{natural}} \cdot (T_{\text{Case}} - T_{\text{air}}) \tag{2.16}$$

where $T_{\text{adia\_case}}$ is the fluid temperature after adiabatic compression in case volume calculated in the thermodynamic module and k_{natural} is the overall natural heat-transfer coefficient of the pump housing surface.

The value of k_{natural} is proportional to the housing surface, which is proportional to the second order of the linear scaling factor λ as usually used for pump design:

$$k_{\text{natural}} = C_{\text{natural\_ref}} \cdot \lambda^2 \ [\text{W/K}] \tag{2.17}$$

where $C_{\text{natural\_ref}}$ is a constant value determined based on steady-state measurements of a baseline unit. The term λ^2 scales the overall natural heat-transfer coefficient with the heat-transfer surface area.

The linear scaling factor λ has been introduced to allow for general use of the model, i.e. without the need of steady-state measurement data for each unit size.

The linear scaling factor can be obtained as:

$$\lambda = \sqrt[3]{\frac{V_i}{V_{i\_\text{baseline}}}} \tag{2.18}$$

where V_i is the displacement volume of the pump or motor under investigation and V_{i_baseline} represents the displacement volume of the baseline unit the steady-state measurements were taken from.

The rate of heat flow from solid parts to both the displacement chamber volume and the case volume can be calculated as:

$$\begin{aligned}\dot{q}_{s\_\mathrm{DC}} &= k_{\mathrm{DC}} \cdot (T_{\mathrm{solid}} - T_{\mathrm{DC}}) \\ \dot{q}_{s\_\mathrm{Case}} &= k_{\mathrm{Case}} \cdot (T_{\mathrm{solid}} - T_{\mathrm{Case}})\end{aligned} \tag{2.19}$$

where k_{DC} and k_{Case} are the overall heat-transfer coefficients of the displacement chamber surface and the case volume surface, T_{DC} is the temperature in the displacement chamber which approximately equals to the average of the inlet flow temperature and the outlet flow temperature.

The value of k_{DC} is a function of Reynolds number on the heat-transfer surface in the displacement chamber which is proportional to the outlet flow rate and the linear scaling factor:

$$k_{\mathrm{DC}} = \left(\frac{Q_{\mathrm{out}}}{\lambda}\right)^{0.4} \cdot \lambda^2 \cdot C_{\mathrm{DC\_ref}} \tag{2.20}$$

where $C_{\mathrm{DC\_ref}}$ is a constant value determined based on the steady-state measurement, the scaling reference, and fluid properties. The term $\frac{Q_{\mathrm{out}}}{\lambda}$ scales the overall heat-transfer coefficient of displacement chamber surface with the Reynolds number; the order value 0.4 is found to match the measurements the best, and the term λ^2 scales the overall heat-transfer coefficient with the heat-transfer surface area.

The value of k_{Case} is a function Reynolds number on the heat-transfer surface in the case which is mainly proportional to the pump speed and the linear scaling factor. The leakage flow rate correction factor (lcf) is used here to add the influence of the leakage flow rate on the Reynolds number:

$$k_{\mathrm{Case}} = \left(n \cdot \lambda^2 \cdot \mathrm{lcf}\right)^{0.4} \cdot \lambda^2 \cdot C_{\mathrm{Case\_ref}} \tag{2.21}$$

where $C_{\mathrm{Case\_ref}}$ is a constant value determined based on the steady-state measurement, the scaling reference and fluid property. The term $n \cdot \lambda^2 \cdot \mathrm{lcf}$ scales the overall heat-transfer coefficient of case volume surface with Reynolds number; the order value 0.4 is found that match the measurements the best, and the term λ^2 scales the overall heat-transfer coefficient with the heat-transfer surface area. lcf is a leakage flow rate correction factor which calculates the leakage flow rate influence on the Reynolds number in the case volume. lcf is a function of the pump speed, the case flow rate, and the linear scaling factor:

$$\mathrm{lcf} = \sqrt{1 + \left(\frac{Q_{\mathrm{Case}} \cdot C_{\mathrm{lcf}}}{\lambda^3 \cdot n}\right)^2} \tag{2.22}$$

where C_{lcf} is a constant value based on the scaling reference. The term $\frac{Q_{\mathrm{Case}} \cdot C_{\mathrm{lcf}}}{\lambda^3 \cdot n}$ is the ratio of the fluid velocity contributed by the leakage flow rate over the fluid velocity contributed by the rotation of the rotating group. By assuming the fluid velocity contributed by the rotational motion of the rotating group is perpendicular to the fluid velocity contributed by the leakage flow, a square and a square root are used here to sum this two velocity vectors together assuming they are perpendicular to each other.

There are four heat-transfer constants, $C_{\mathrm{natural\_ref}}$, $C_{\mathrm{DC\_ref}}$, $C_{\mathrm{Case\_ref}}$, and C_{lcf}, needed to complete this model.

C_{lcf} is determined from the geometry of the pump:

$$C_{\mathrm{lcf}} = \frac{\pi \cdot A_{\mathrm{block}} \cdot t}{2} \tag{2.23}$$

where A_{block} represents cylinder block outer surface area and t is the distance between the cylinder block outer surface and the housing inner surface.

$C_{\mathrm{natural\_ref}}$ is determined from the geometry of the pump and the air-metal natural convection heat-transfer coefficient of the outer housing surface:

$$C_{\mathrm{natural\_ref}} = h_{c\_\mathrm{air}} \cdot A_{\mathrm{housing}} \tag{2.24}$$

where $h_{\mathrm{c\_air}}$ is a the air-metal natural convection heat-transfer coefficient and A_{housing} is the outer housing surface area.

$C_{\mathrm{DC\_ref}}$ and $C_{\mathrm{Case\_ref}}$ are found by conducting optimization on the discrepancies between the simulated pump flow temperatures and the steady-state measured pump flow temperatures.

Those resulting constants can be used for any given size of swash plate-type axial piston pump or motor by using the linear scaling law.

Concluding the rate of heat flow balance in the pump heat-transfer model:

$$\begin{aligned}\dot{q}_{s\_\mathrm{DC}} &= \dot{q}_{s\_\mathrm{DC}}(T_{\mathrm{solid}}, T_{\mathrm{out}}) \\ \dot{q}_{s\_\mathrm{Case}} &= \dot{q}_{s\_\mathrm{Case}}(T_{\mathrm{solid}}, T_{\mathrm{Case}}) \\ \dot{q}_{\mathrm{DC}} &= \dot{q}_{\mathrm{DC}}(T_{\mathrm{solid}}, T_{\mathrm{out}}) \\ \dot{q}_{\mathrm{Case}} &= \dot{q}_{\mathrm{Case}}(T_{\mathrm{solid}}, T_{\mathrm{Case}})\end{aligned} \tag{2.25}$$

There are three heat flow rate balance equations:

$$\begin{cases} \dot{q}_{\mathrm{loss}} = \dot{q}_{s\_\mathrm{DC}} + \dot{q}_{s\_\mathrm{Case}} \\ \dot{q}_{\mathrm{DC}} = \dot{q}_{s\_\mathrm{DC}} \\ \dot{q}_{\mathrm{Case}} = \dot{q}_{s\_\mathrm{Case}} \end{cases} \tag{2.26}$$

with three unknowns T_{out}, T_{Case}, and T_{solid}.

2.3. *Pump port and case flow temperatures prediction model inputs*

The thermal model requires two types of inputs, the fluid properties, and the operating conditions.

The required fluid properties include the density, the specific heat capacity, and the heat-transfer constants which were discussed in the previous section. Note the heat-transfer constants have been found based on steady-state measurements of a baseline unit. Linear scaling factors are needed to apply them for different unit sizes. Table 2 summarizes the required fluid properties:

The required operating conditions include the pump size, the pump speed, the inlet pressure, the outlet pressure, the case pressure, the inlet temperature, the ambient temperature, the outlet flow rate, the case flow rate, and

Table 2. Required fluid properties.

Fluid Properties		Comments
Density	ρ	Function of pressure and temperature
Specific heat capacity	c_p	Function of temperature

the total power loss. Note that the pump size is used to calculate the linear scaling factor, and the displacement is reflected in the outlet flow rate. The outlet flow rate, the case flow rate, and the total power loss cannot be obtained directly from the pump design; hence, the FSTI simulation model has to be used to estimate these values. An iterative process is required between solving the proposed outlet and case temperature model and the FSTI simulation model to determine the remaining parameters, as shown in Figure 9. Table 3 summarizes the required operating conditions:

2.4. *Pump outlet port and case flow temperatures prediction model solution scheme*

The pump flow temperatures prediction model calculates the outlet port temperature and the case flow temperature for the given pump size at given operating conditions, for a given fluid, and the estimated power loss of the pump or motor. The thermodynamic module calculates the outlet flow temperature variation and the case temperature variation by assuming adiabatic compression or expansion as the first step. In a second step, the heat-transfer module is used to correct the outlet flow temperature and the case flow temperature considering the heat-transfer.

However, the outlet flow temperature and the case flow temperature are needed to specify the fluid properties used in the pump flow temperatures prediction model. The pump flow temperatures prediction model solution scheme is shown in Figure 8. The fluid properties which are functions of temperature are initialized by applying the inlet flow temperature, and updated by applying the outlet flow temperature and the case flow temperature obtained from the pump port and case flow temperatures prediction model at each iteration step, until both the outlet flow temperature and the case flow temperature converge.

Table 3. Required operating conditions.

Operating conditions		Comments
Pump size	V_i	Known
Pump speed	n	Known
Inlet pressure	p_{in}	Known
Outlet pressure	p_{out}	Known
Case pressure	p_{Case}	Known
Inlet temperature	T_{in}	Known
Ambient temperature	T_{air}	Known
Outlet flow rate	Q_{out}	FSTI
Case flow rate	Q_{Case}	FSTI
Power loss	$\dot{q}_{\text{loss}}$	FSTI

The pump power loss can be estimated using an extended version of Maha's FSTI simulation program. The FSTI model calculates the energy dissipation in the three main lubricating gaps of a swash plate-type axial piston machine. As already explained in the introduction of this paper, the precise calculation of energy dissipation in the three lubricating interfaces of swash plate-type axial piston machines requires port and case temperatures as inputs in order to use them as thermal boundaries to solve for non-isothermal flow in the fluid film and also to consider the deformation of solid parts due to thermal loading and its impact on fluid film thickness and energy dissipation in these three lubricating interfaces. More details about this fluid–structure interaction model and the in-house developed program can be found in Pelosi and Ivantysynova (2012), Zecchi and Ivantysynova (2013) and Schenk and Ivantysynova (2014). The FSTI model has been extended with a 'churning loss model' and a 'remaining loss estimator model.' The remaining loss estimator model is used to estimate the losses created in the shaft bearing and the shaft sealing.

In order to estimate the total power loss of a given swash plate axial piston machine, a co-simulation between the extended FSTI program and the port and case temperature prediction program is required. The iterative simulation scheme of the coupled models is shown in Figure 9. The extended FSTI model can be used to calculate the outlet flow rate, the case flow rate, and the total power losses for a given pump design, given inlet port temperature, given fluid properties, and estimated outlet port and case flow temperatures. In a second step, the pump outlet port and case flow temperature prediction model is used to calculate the outlet port temperature and the case flow temperature based on the power loss and the outlet and case flow rate from the FSTI model. In a third step, the obtained outlet port and case flow temperature will be used to rerun the extended FSTI model to update the power loss and the outlet and case flow rate. The described iteration cycle between the two models will be repeated until the outlet and case flow temperature converge.

3. Comparison study to measurements

In order to verify the accuracy of the proposed pump outlet port and case flow temperatures prediction model, four sets of measurement data have been used for comparison, which include four different pump designs with different maximum displacement volumes and working with different fluids and at different pressures, speeds, and at different swash plate angles.

All the measurement data which were used for this study are summarized in Table 4:

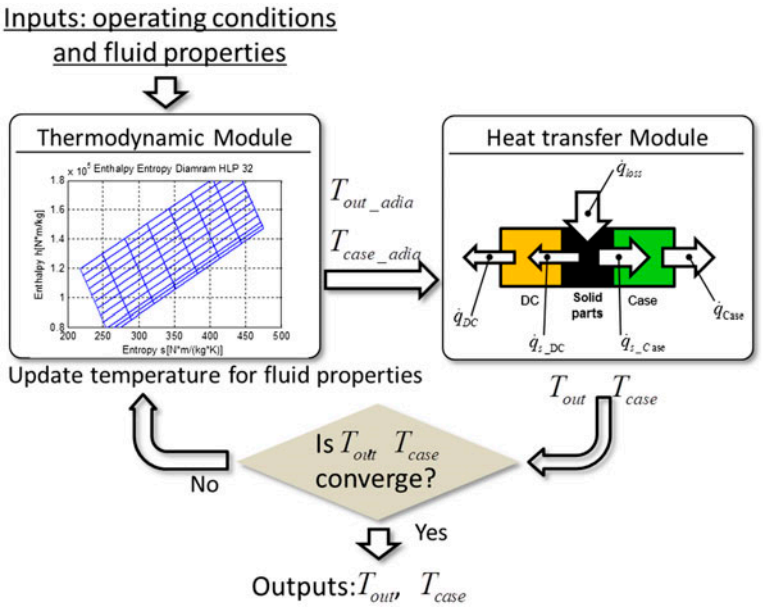

Figure 8. Pump flow temperatures prediction model solution scheme.

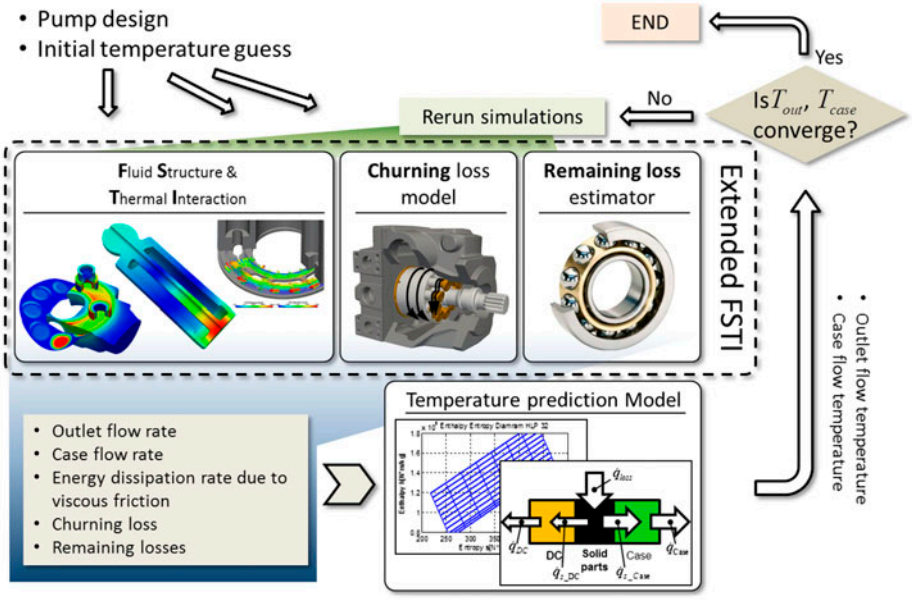

Figure 9. Pump flow temperatures prediction model coupled with FSTI.

Table 4. Measurement sets for comparison.

Set #	Fluid type	Pump size [cc]	Displacement [%]	Pump speed [rpm]	Pressure differential [bar]
1	Type I	42	100, 80, 60, 40, 20	200, 500, 1000, 2000, 3000, 4000, 4600	20, 50, 100, 200, 300, 400
2	Type I	130	100, 50, 20	1000, 2000, 2800	50, 100, 200, 300, 400
3	Type I	75	100, 20	500, 1000, 1500, 2000, 2800	100, 200, 300, 400
4	Type II	4	100, 10	8750, 10500	200

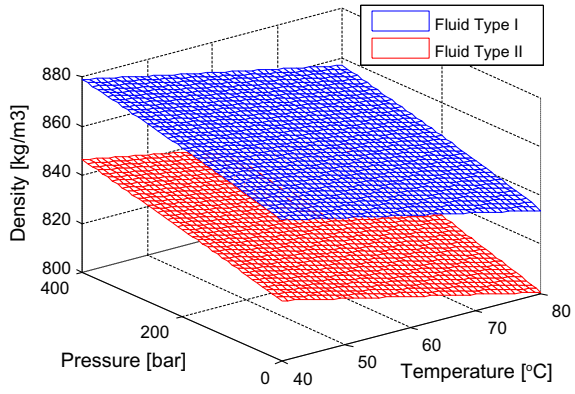

Figure 10. Densities of both types of fluid.

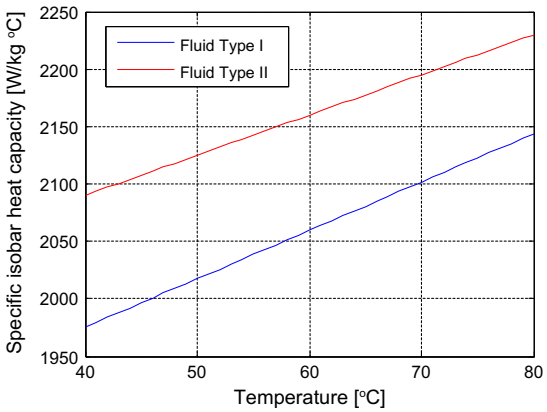

Figure 11. Specific isobar heat capacities for both types of fluid.

3.1. *Fluid properties*

Two types of hydraulic fluids have been used within this study.

Figure 10 shows the density change with pressure and temperature for both types of fluid. Two meshes in the figure are almost parallel with each other and have about 35 kg/m^3 offset.

Figure 11 shows the change of the specific isobaric heat capacity with temperature.

3.2. *Overall heat-transfer coefficients*

The value of the overall heat-transfer coefficients for the displacement chamber surface, the case volume surface, and the overall air natural heat-transfer coefficient of the housing surface are calculated from Equations (2.20), (2.21), and (2.17). The constant values C_{DC_ref}, C_{Case_ref}, and $C_{natural\_ref}$ are determined based on the steady-state measurement of a 130 cc pump which has been used as a baseline/scaling reference for the comparison study.

The linear scaling factors λ, which have been used for different sizes of pumps in the comparison study are summarized in Table 5.

Table 5. Linear scaling factor λ.

Pump size [cc]	Linear scaling factor λ
42	0.69
130	1.00
75	0.83
4	0.31

Table 6. Comparison result for 130 cc pump at 100% displacement.

Beta	n	Δp	T_out			T_case		
			measured	*simulated*	*difference*	*measured*	*simulated*	*difference*
[%]	[%]	[%]	[°C]	[°C]	[°C]	[°C]	[°C]	[°C]
100	35.7	12.5	53.1	53.1	-0.1	63.2	60.7	2.5
100	35.7	25	54.1	54.1	0.0	66.7	68.0	-1.3
100	35.7	50	56.0	55.9	0.1	71.7	74.5	-2.8
100	35.7	75	58.2	58.0	0.2	76.0	82.2	-6.2
100	35.7	100	60.5	60.4	0.1	79.4	80.9	-1.5
100	71.5	12.5	53.7	53.7	0.0	76.6	76.2	0.4
100	71.5	25	54.6	54.6	0.0	78.4	79.5	-1.1
100	71.5	50	55.8	55.8	0.0	80.1	80.8	-0.8
100	71.5	75	57.8	57.7	0.0	83.1	86.8	-3.8
100	71.5	100	59.6	59.6	-0.1	84.3	83.8	0.5
100	100	12.5	57.2	57.2	0.0	83.1	83.9	-0.8
100	100	25	59.0	59.0	0.0	87.5	85.3	2.2
100	100	50	62.4	62.4	0.0	90.2	89.6	0.6
100	100	75	67.5	67.5	0.0	94.3	95.5	-1.2

Table 7. Comparison result for 130 cc pump at 50% displacement.

Beta	n	Δp	T_out			T_case		
			measured	*simulated*	*difference*	*measured*	*simulated*	*difference*
[%]	[%]	[%]	[°C]	[°C]	[°C]	[°C]	[°C]	[°C]
50	35.7	12.5	53.4	53.5	-0.1	60.9	58.4	2.4
50	35.7	25	54.6	54.6	0.0	62.5	62.3	0.2
50	35.7	50	57.2	56.9	0.2	66.8	71.6	-4.7
50	35.7	75	60.3	59.7	0.5	72.1	78.2	-6.1
50	35.7	100	63.9	63.9	0.0	79.6	79.7	-0.1
50	71.5	12.5	53.7	53.7	0.0	73.9	72.3	1.7
50	71.5	25	54.6	54.6	0.0	74.3	73.4	0.9
50	71.5	50	56.7	56.6	0.1	75.1	78.9	-3.7
50	71.5	75	58.9	58.7	0.2	77.5	82.7	-5.2
50	71.5	100	61.2	61.2	0.0	81.6	81.4	0.1
50	100	12.5	53.7	53.8	-0.1	81.8	75.4	6.4
50	100	25	54.6	54.7	-0.1	82.2	78.3	3.8
50	100	50	56.6	56.6	-0.1	82.3	81.3	1.1
50	100	75	58.6	58.6	0.1	83.2	84.4	-1.1
50	100	100	60.4	60.6	-0.1	84.9	82.6	2.3

3.3. *Comparison results*

Following figures and tables show the comparison results of the model to four sets of measurements. Since the comparison results to the set #1 measurement cover a

Table 8. Comparison result for 130 cc pump at 20% displacement.

Beta	n	Δp	T_out			T_case		
			measured	*simulated*	*difference*	*measured*	*simulated*	*difference*
[%]	[%]	[%]	[°C]	[°C]	[°C]	[°C]	[°C]	[°C]
20	35.7	12.5	54.1	54.2	-0.1	60.6	59.9	0.7
20	35.7	25	56.1	55.9	0.2	63.4	65.2	-1.8
20	35.7	50	61.4	60.5	0.9	69.5	72.7	-3.2
20	71.5	12.5	54.3	54.4	-0.1	73.1	71.9	1.1
20	71.5	25	55.5	55.5	0.0	73.3	72.8	0.4
20	71.5	50	58.6	58.2	0.4	74.4	77.8	-3.4
20	71.5	75	62.6	61.9	0.7	78.1	81.6	-3.5
20	71.5	100	67.6	69.0	-1.4	85.5	83.0	2.5
20	100	12.5	54.7	54.7	0.0	81.1	81.7	-0.6
20	100	25	55.7	55.7	-0.1	80.8	80.1	0.7
20	100	50	57.9	57.8	0.0	80.7	81.6	-0.9
20	100	75	61.3	60.9	0.4	82.3	84.9	-2.6
20	100	100	65.5	66.1	-0.6	86.9	85.0	1.9

large amount of different operating conditions, 3D graphs have been chosen to present the results. In those graphs, the x axis and the y axis represent the pressure differential and the rotating speed, and the z axis shows the temperature. The remaining three model comparison results are shown in tables.

The pressure differential and the pump speed have been normalized to maximum pressure and maximum speed for each set of measurements.

The power losses which are used in the pump flow temperatures prediction model have been calculated from the measurements:

$$\dot{q}_{\text{loss}} = \dot{m}_{\text{out}} \cdot C_p \cdot (T_{\text{out}} - T_{\text{out\_adia}}) + \dot{m}_{l,e} \cdot C_p \cdot (T_{\text{Case}} - T_{\text{Case\_adia}}) \tag{3.1}$$

The calculated power loss reflects the required power loss to heat up the outlet flow and case flow to the measured outlet port and case temperatures.

3.3.1. *Set#1: 42 cc pump with fluid type I*

Figures 12–21 show the comparison results of both the outlet flow temperature and the case flow temperature.

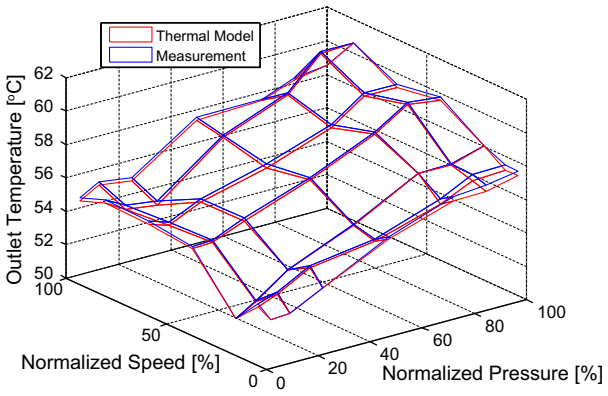

Figure 12. Outlet flow temperature comparison at 100% displacement.

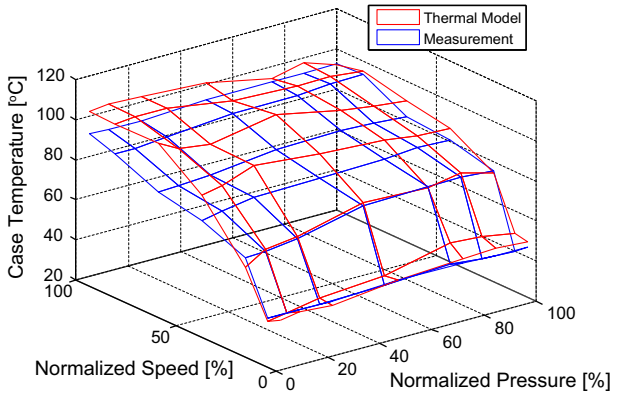

Figure 13. Case flow temperature comparison at 100% displacement.

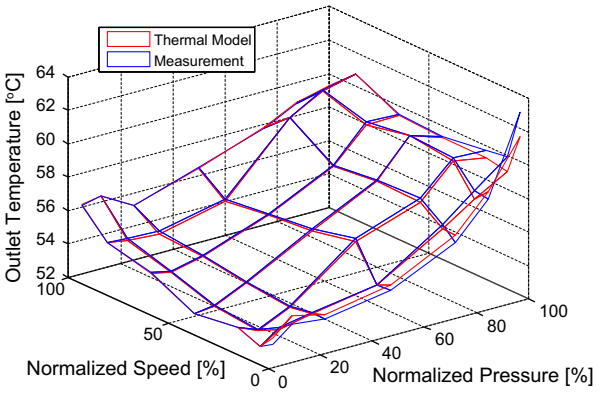

Figure 14. Outlet flow temperature comparison at 80% displacement.

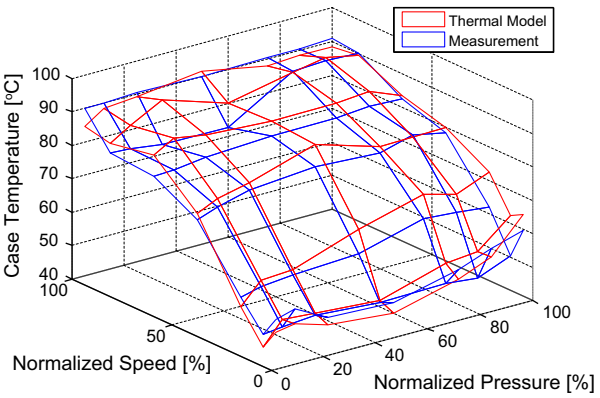

Figure 15. Case flow temperature comparison at 80% displacement.

The red meshes show the simulated temperature, and the blue meshes show the measured temperature.

3.3.2. *Set#2: 130 cc pump with fluid type I*

Tables 6–8 show the comparison results to the measurements on a 130 cc pump with the fluid type I. The first

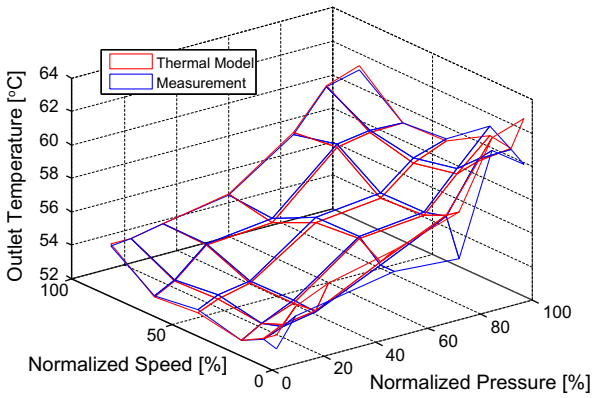

Figure 16. Outlet flow temperature comparison at 60% displacement.

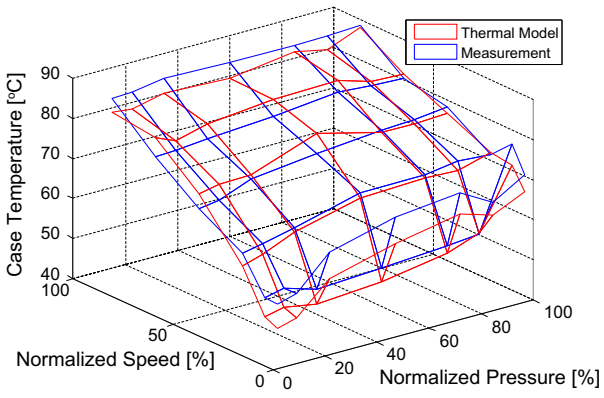

Figure 19. Case flow temperature comparison at 40% displacement.

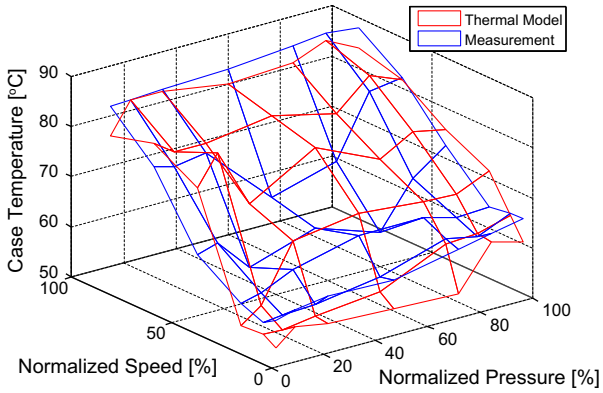

Figure 17. Case flow temperature comparison at 60% displacement.

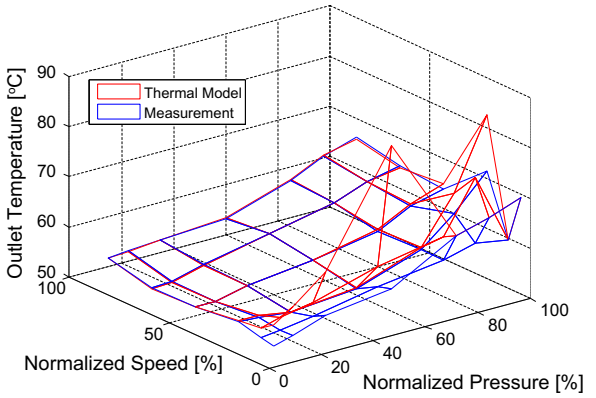

Figure 20. Outlet flow temperature comparison at 20% displacement.

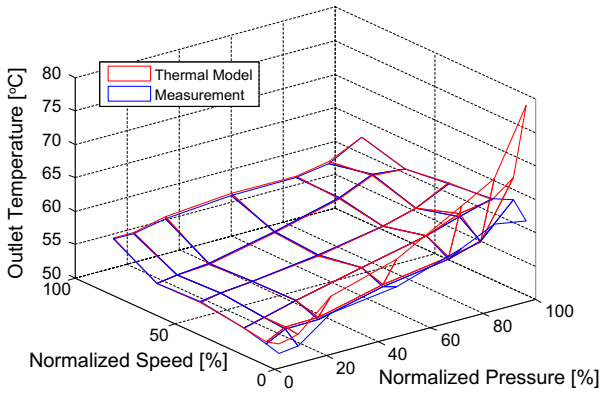

Figure 18. Outlet flow temperature comparison at 40% displacement.

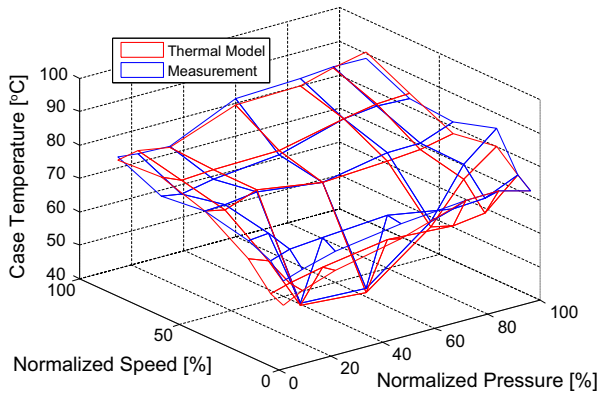

Figure 21. Case flow temperature comparison at 20% displacement.

three include the swash plate angle, the pump speed, and the pressure differential in percentage to the maximum value. The last six columns show the comparison results which include the measured port and case temperatures, the simulated port and case temperatures, and the difference between the measurement and the simulation.

3.3.3. *Set#3: 75 cc pump with fluid type I*

Tables 9 and 10 show the comparison results to the measurements of a 75 cc pump with fluid type I. The first three columns include the swash plate angle, the pump speed, and the pressure differential in percentage to the maximum value. The last six columns are the measured

Table 9. Comparison result for 75 cc pump at 100% displacement.

Beta	n	Δp	T_out			T_case		
			measured	*simulated*	*difference*	*measured*	*simulated*	*difference*
[%]	[%]	[%]	[°C]	[°C]	[°C]	[°C]	[°C]	[°C]
100	17.9	25	54.2	54.0	0.2	48.0	57.9	-9.9
100	17.9	50	56.0	55.7	0.3	53.8	63.8	-10.0
100	17.9	75	58.4	58.0	0.4	61.0	68.9	-7.9
100	35.7	25	54.2	54.1	0.1	56.8	68.6	-11.9
100	35.7	50	55.8	55.6	0.1	60.5	69.5	-9.0
100	35.7	75	57.4	57.3	0.2	64.0	71.0	-6.9
100	35.7	100	59.4	59.4	0.0	70.2	69.9	0.3
100	53.6	25	54.3	54.2	0.1	58.7	71.6	-12.9
100	53.6	50	55.8	55.6	0.1	61.7	71.7	-10.0
100	53.6	75	57.4	57.3	0.1	65.8	71.1	-5.3
100	71.5	25	53.8	53.7	0.1	63.5	74.0	-10.5
100	71.5	50	55.4	55.3	0.1	66.7	74.2	-7.5
100	71.5	75	57.1	57.0	0.1	69.2	72.3	-3.0
100	71.5	100	58.6	58.7	-0.1	73.0	69.5	3.5
100	100	75	57.3	57.3	0.0	75.0	73.5	1.5
100	100	100	58.7	58.9	-0.2	76.4	71.1	5.2

Table 10. Comparison result for 75 cc pump at 20% displacement.

Beta	n	Δp	T_out			T_case		
			measured	*simulated*	*difference*	*measured*	*simulated*	*difference*
[%]	[%]	[%]	[°C]	[°C]	[°C]	[°C]	[°C]	[°C]
100	35.7	25	55.1	55.5	-0.4	60.1	58.6	1.5
100	35.7	75	64.1	66.2	-2.1	70.9	68.9	1.9
100	71.5	25	54.8	54.8	0.0	60.0	59.6	0.4
100	71.5	75	59.9	60.1	-0.2	68.2	67.5	0.7
100	71.5	100	66.1	69.8	-3.7	76.2	73.1	3.2
100	100	75	61.5	61.3	0.2	71.4	72.0	-0.6
100	100	100	65.8	67.1	-1.3	76.8	75.0	1.8

temperatures, the simulated temperatures, and the difference between the measurement and the simulation.

3.3.4. Set#4: 4 cc pump with fluid type II

Table 11 shows the comparison results to the measurements conducted on a 4 cc pump with fluid type II. The first three columns are the swash plate angle, the pump speed, and the pressure differential in percentage of the maximum value. The last six columns are the measured temperatures, the simulated temperatures, and the difference between the measurement and the simulation.

Table 11. Comparison result for 4 cc pump with another type of fluid.

Beta	n	Δp	T_out			T_case		
			measured	*simulated*	*difference*	*measured*	*simulated*	*difference*
[%]	[%]	[%]	[°C]	[°C]	[°C]	[°C]	[°C]	[°C]
100	83.3	100	86.2	86.2	0.0	96.1	96.8	-0.8
10	83.3	100	88.0	88.1	-0.1	97.0	96.7	0.3
100	83.3	100	119.6	119.5	0.0	125.2	125.8	-0.6
10	83.3	100	120.6	121.1	-0.5	125.3	124.5	0.8
100	100	100	86.6	86.7	0.0	99.7	98.8	0.9
10	100	100	90.0	90.3	-0.3	101.8	101.1	0.8
100	100	100	119.8	119.7	0.1	127.2	128.7	-1.5
10	100	100	120.7	120.8	-0.1	127.6	127.5	0.1

3.4. Conclusion of the comparison study

The comparison study verified that the proposed pump outlet port and case flow temperatures prediction model is able to predict the outlet port flow temperature and the case flow temperature with a reasonable accuracy of ±5 °C for outlet flow temperature and ±10 °C for case flow temperature. This accuracy is sufficient for the use of the model as input parameter estimator for the FSTI simulation model.

4. Sensitivity study

In order to save simulation time and effort within a computational pump design utilizing the proposed iterative method of coupling the pump outlet port and case flow prediction model with the extended FSTI model as briefly discussed in chapter 2, a study has been conducted to investigate the sensitivity of pump outlet flow and case flow temperature on torque loss, volumetric loss, and operating conditions of a given pump. The outcome of this sensitivity study will be used as guidance for estimation of temperature boundary conditions (outlet and case flow temperature) within a computational design process. With other words, the sensitivity study was conducted to determine in which cases the impact of design change on port and case flow temperatures is significant and/or negligible.

In this sensitivity study, the internal leakage was ignored due to its minor impact on the pump port and case flow temperatures. The outlet mass flow rate follows the simplified equation:

$$\dot{m}_{\text{out}} = \dot{m}_{\text{th}} - \dot{m}_{\text{leakage}} \tag{4.1}$$

The theoretical flow rate is calculated from the pump size and the operating condition.

The total power loss is simplified into two parts, the volumetric power loss and the mechanical power loss. The volumetric power loss is generated by the leakage flow rate and the pressure drop from the displacement chamber pressure to the case pressure, and the mechanical power loss captures all the rest of the energy dissipation rate.

$$\begin{aligned} P_{\text{loss}} &= P_{\text{volumetric}} + P_{\text{mechanical}} \\ P_{\text{loss}} &= Q_{\text{leakage}} \cdot \Delta p + P_{\text{mechanical}} \end{aligned} \tag{4.2}$$

4.1. Sensitivity study on leakage and mechanical loss

Fifty sets of outlet flow temperatures and case flow temperatures were obtained at different leakage flow rates and mechanical losses using the pump outlet port and case flow temperatures prediction model. Figures 22 and 23

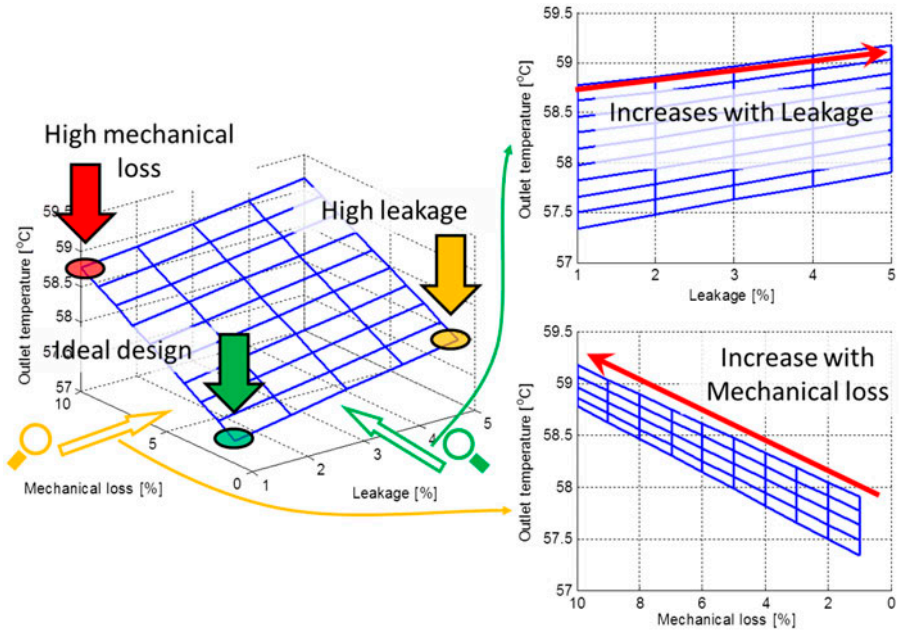

Figure 22. Outlet flow temperatures for different leakages and mechanical losses.

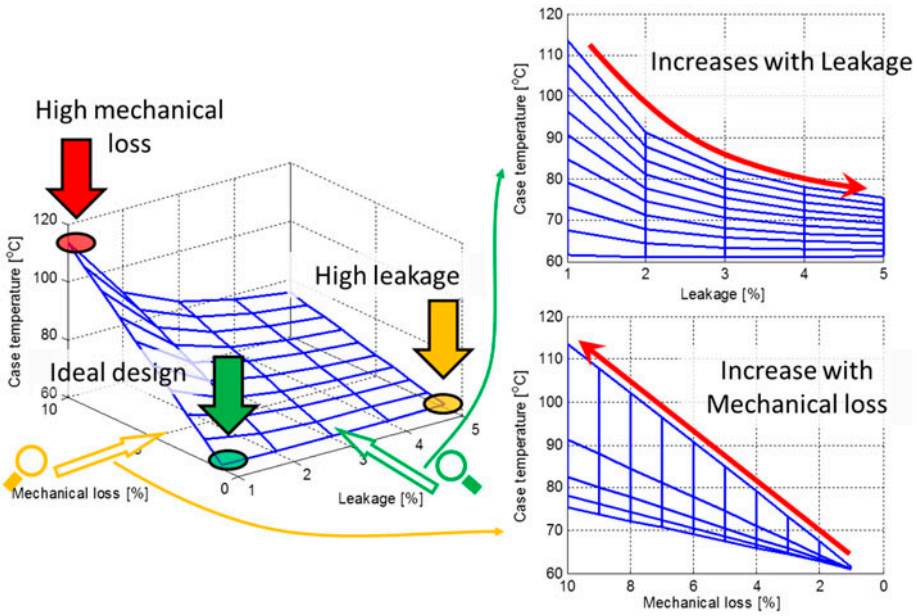

Figure 23. Case flow temperatures for different leakages and mechanical losses.

show two 3D meshes for the simulated outlet flow temperatures and case flow temperatures.

In Figure 22, the 3D mesh shows the outlet flow temperatures over different leakages and mechanical losses. The leakages displayed in the picture are normalized to the theoretical delivered flow rate, and the mechanical losses displayed in the picture are normalized to the theoretical delivered power.

The green dot in the 3D picture shows the ideal design which has minimum leakage and minimum mechanical loss. The design marked with red dot has high mechanical loss, and the design marked with yellow dot has high leakage.

The two pictures on the right-hand side show two side views of the 3D picture. From these pictures, two trends can be observed clearly: the outlet flow temperature increases with both the leakage and the mechanical loss.

Figure 23 shows the case flow temperatures over different leakages and mechanical losses. Two trends can

be clearly observed for the case flow temperature: the case flow temperature decreases with the leakage and increases with the mechanical loss.

The higher mechanical power loss transferred into the displacement chamber volume and the case volume increases both the outlet flow temperature and the case temperature.

The case flow temperature decreases with the leakage because the case flow temperature variation is inversely proportional to the case flow rate which is leakage flow rate. The outlet flow temperature increases with the leakage because higher leakage produces higher total power loss.

Figure 23 also shows that the case flow temperature mesh is flat in the high leakage region and steeper in the low leakage region. This is because the sensitivity of the case flow temperature decreases with increasing case flow rate, i.e. increasing leakage.

Figure 24 shows an example of using the sensitivity study to guide the initial temperature guess. For example, if the design goal is to reduce the leakage flow rate of a pump from point 1 to point 2 by optimizing the pump design. The sensitivity study results in Figure 24 show that the case temperatures at point 1 and point 2 are almost the same. Thus, the case temperature at point 1 can be used as the initial case temperature guess at point 2. In case of an original pump design with higher mechanical loss which places the original design at point 3, and the pump design optimization should reduce the leakage from point 3 to point 4, the impact on case temperature is not negligible. Thus, higher case temperature should be used as the initial case temperature guess.

4.2. *Sensitivity study on displacement*

In the sensitivity study on displacement, the outlet flow temperature and the case flow temperature were predicted at 100, 50, and 20% displacement over a larger range of leakage and mechanical loss.

Figures 25 and 26 show the outlet flow temperature meshes and case flow temperature meshes at 100, 50, and 20% displacement. The crosses and circles on the meshes in Figure 25 and Figure 26 show the measured temperatures and the simulated temperatures at corresponding operating conditions. The simulated temperatures are very close to the measured temperatures which indicate that the temperature meshes obtained from the simulation are accurate enough to represent the sensitivity of the real pump.

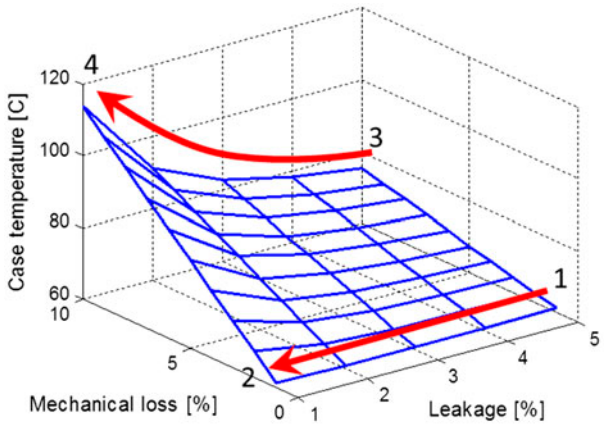

Figure 24. Case flow temperatures for different leakages and mechanical losses.

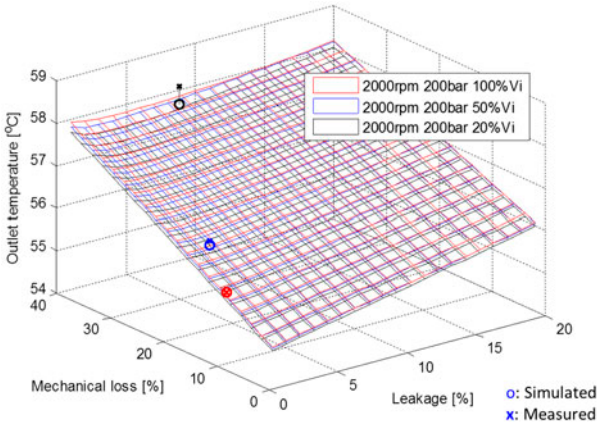

Figure 25. Outlet flow temperature meshes for different displacements @ 2000 rpm and 200 bar.

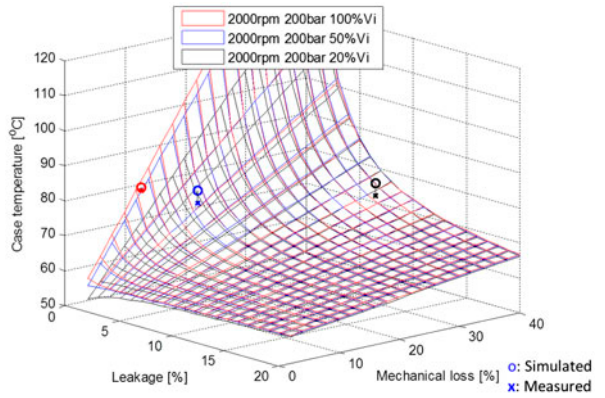

Figure 26. Case flow temperature meshes for different displacements @ 2000 rpm and 200 bar.

Both Figures 25 and 26 show that the temperature meshes for different displacements are very close to each other. However, the measured temperature points indicate that the pump has very different normalized leakages and normalized mechanical losses for different displacements. This concludes that the different thermal behaviors of the pump running at different displacements are mainly caused by the different normalized leakages and normalized mechanical losses.

4.3. *Sensitivity study on pressure differential*

Figures 27 and 28 show the outlet flow temperature meshes and case flow temperature meshes for 400 bar

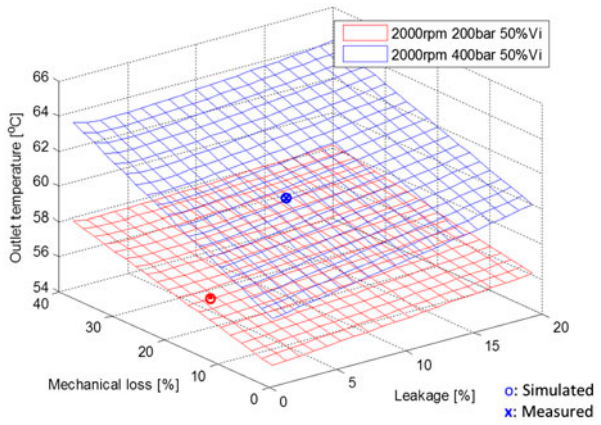

Figure 27. Outlet flow temperature meshes for different pressure differentials @ 2000 rpm and 50% V_i.

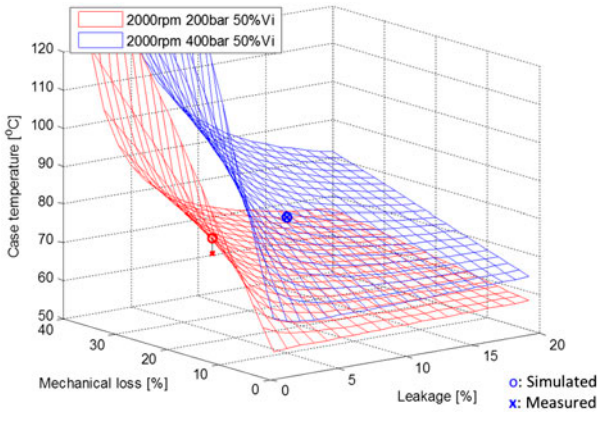

Figure 28. Case flow temperature meshes for different pressure differentials @ 2000 rpm and 50% V_i.

pressure differential and 200 bar pressure differential between the outlet and inlet. Again, the measured temperature and the corresponding simulated temperature can be found in these figures.

Figure 27 shows that the outlet flow temperature meshes are very different for different pressure differentials. That is because the temperature variation is proportional to the pressure change. The fluid temperature will increase more when running at higher pressure differential.

Figure 28 shows that the case flow temperature mesh at higher pressure differential is higher than the mesh at lower pressure differential. This is because at the same leakage and mechanical loss point, the pump running at higher pressure differential will have higher power loss.

4.4. *Sensitivity study on pump speed*

Figures 29 and 30 show the outlet flow temperature meshes and case flow temperature meshes at 1000, 2000, and 2800 rpm. Again, the measured temperatures and the simulated temperatures are marked.

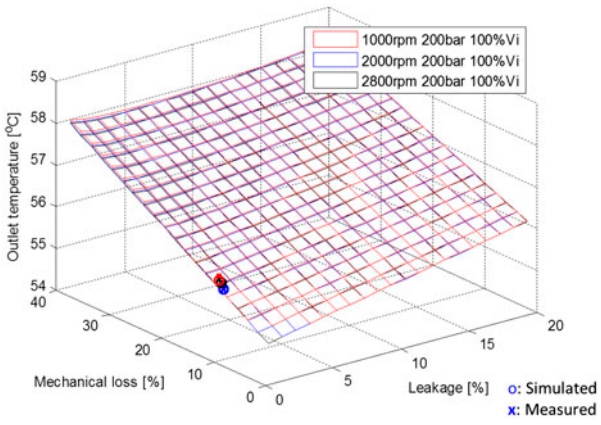

Figure 29. Outlet flow temperature meshes for different pump speeds @ 200 bar and 100% V_i.

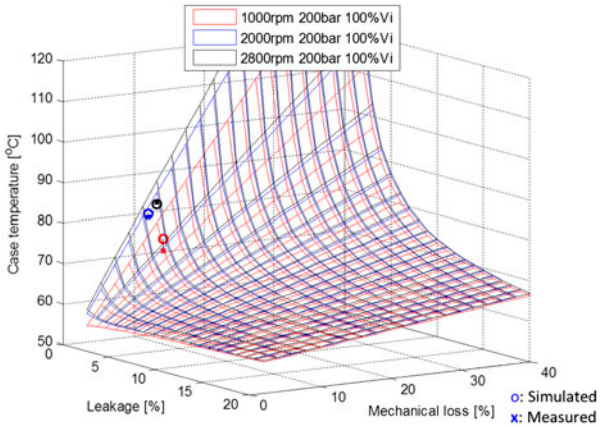

Figure 30. Case flow temperature meshes for different pump speeds @ 200 bar and 100% V_i.

Figure 29 shows that the outlet flow temperature meshes for different pump speeds are very close to each other. The measurement points show that the normalized leakages and the normalized mechanical losses are very similar at different pump speeds as well. The pump running at different pump speeds will have a similar outlet port flow temperature.

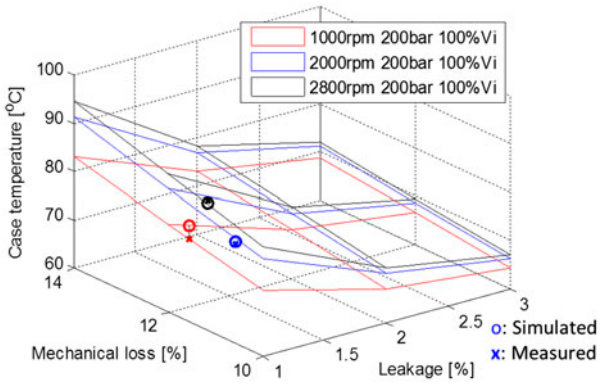

Figure 31. Zoomed in Figure 30 of case flow temperature meshes for different pump speeds.

Figure 30 shows that the case flow temperature meshes for different pump speeds are very close to each other in the high leakage region and differ more in the low leakage region. The three measurement points are located in the low leakage region. Figure 31 shows the zoomed area of measured and simulated points of the case flow temperature for different pump speeds. Even though the pump running at different speeds has similar normalized leakages and normalized mechanical losses, the different thermal behaviors due to the different pump speeds separate the case temperature points vertically, which can be observed in Figure 31.

For all different speeds, the power losses are proportional not only to the pump speeds, but also to the outlet flow rates and the case flow rates. That explains why the pump flow temperature meshes of the pump running at different speeds are nearly identical in the high leakage region. The case flow temperature meshes show differences in the low leakage region because the low case flow rate causes an increase in the case temperature.

The temperature of solid parts of the pump running at higher speed is higher due to the higher power loss. Since normally the temperature in the case volume is higher than the temperature in the displacement chamber volume, the ratio of solid-case temperature differential over solid-DC temperature differential $\frac{T_{solid}-T_{Case}}{T_{solid}-T_{DC}}$ increases with the solid parts temperature. Furthermore, the ratio of the solid-case heat-transfer rate over the solid-DC heat-transfer rate $\frac{\dot{q}_{s\_Case}}{\dot{q}_{s\_DC}}$ also increases with the solid parts temperature. That explains why the pump running at higher speed has higher case flow temperature.

Additional to that the pump running at lower speed has lower power loss but has almost the same natural convection heat flow rate into the air. Therefore, the pump running at lower speed has relatively greater heat-transfer ratio into the air but not into the fluid.

4.5. *Conclusion of the sensitivity study*

The present study captures the sensitivity of the pump thermal behavior over the normalized leakage flow rate, the normalized mechanical loss, the displacement, the pressure differential, and the pump speed. The outlet port flow temperature increases with both the leakage and the mechanical loss, and the case flow temperature decreases with the leakage and increases with the mechanical loss. The sensitivity of the case flow temperature decreases with the leakage. The impact of pump displacement on port and case temperature is mainly caused by the different normalized leakages and normalized mechanical losses. The impact of pump pressure differential on port and case temperature differential is mainly caused by the temperature variations due to the pressure changes. The impact of pump speed on port and case temperature is mainly caused by the heat-transfer characteristic.

6. Conclusion

The proposed pump outlet and case flow temperatures prediction model, which considers both the temperature variation due to the compression or expansion and heat-transfer due to energy dissipation/power loss, is able to predict the outlet port flow temperature and the case flow temperature for any given pump or motor size at any given operating condition based on the given total power loss and the leakage flow rate with reasonable accuracy. The results (outlet port and case temperature) can be used as input parameter for the in-house developed FSTI simulation program, which solves for non-isothermal gap flow considering elasto-hydrodynamic effects due to thermal and pressure loading of the main pump surfaces forming the lubricating interfaces.

The pump outlet and case flow temperatures prediction model coupled with the FSTI model can be used for computational design of new pumps or optimization of given designs without the need of measured port and case temperature data.

The results of the conducted sensitivity study can be used to reduce the required computation time for port and case temperature estimation as a boundary condition for FSTI model, thus can help to shorten the design process while keeping required prediction accuracy.

Nomenclature

C_{Case_ref}	Case heat-transfer constant	[–]
C_{DC_ref}	DC heat-transfer constant	[–]
C_{lcf}	Leakage flow rate correction factor constant	[–]
$C_{natural\_ref}$	Natural heat-transfer constant	[–]
c_p	Specific heat capacity	$\left[\frac{J}{kg \cdot K}\right]$
h	Enthalpy	$\left[\frac{J}{kg}\right]$
k_{Case}	Overall case heat-transfer coefficient	$\left[\frac{W}{K}\right]$
k_{DC}	Overall DC heat-transfer coefficient	$\left[\frac{W}{K}\right]$
$k_{natural}$	Overall natural heat-transfer coefficient	$\left[\frac{W}{K}\right]$
λ	Linear scaling factor	[–]
lcf	Leakage flow rate correction factor	[–]
$\dot{m}_{Case}$	Case mass flow rate	$\left[\frac{kg}{s}\right]$
$\dot{m}_{in}$	Inlet mass flow rate	$\left[\frac{kg}{s}\right]$
$\dot{m}_{out}$	Outlet mass flow rate	$\left[\frac{kg}{s}\right]$
n	Pump speed	[rpm]
p_{Case}	Case pressure	[bar]

p_{in}	Inlet pressure	[bar]
p_{out}	Outlet pressure	[bar]
p_{DC}	DC pressure	[bar]
$\dot{q}_{Case}$	Heat flow rate out of case volume with case flow rate and natural convection	[W]
$\dot{q}_{DC}$	Heat flow rate out of DC volume with outlet flow rate	[W]
$\dot{q}_{loss}$	Total power loss	[W]
$\dot{q}_{s\_Case}$	Heat-transfer rate from solid parts to case volume	[W]
$\dot{q}_{s\_DC}$	Heat-transfer rate from solid parts to DC volume	[W]
Q_{Case}	Case flow rate	$\left[\frac{l}{min}\right]$
Q_{in}	Inlet flow rate	$\left[\frac{l}{min}\right]$
Q_{out}	Outlet flow rate	$\left[\frac{l}{min}\right]$
ρ	Fluid density	$\left[\frac{kg}{m^3}\right]$
s	Entropy	$\left[\frac{J}{kg \cdot K}\right]$
T_{adia_Case}	Case temperature after adiabatic compression/expansion	[°C]
T_{adia_DC}	DC temperature after adiabatic compression/expansion	[°C]
T_{air}	Air temperature	[°C]
T_{Case}	Case temperature	[°C]
T_{DC}	DC temperature	[°C]
T_{in}	Inlet temperature	[°C]
T_{out}	Outlet temperature	[°C]
v	Specific volume	$\left[\frac{m^3}{kg}\right]$
V_i	Pump size	[cc]

Notes on contributors

L. Shang was born on 25 March 1989 in Tianjin (China). He received his BS degree in Thermal Energy and Power Engineering from Huazhong University of Science and Technology in 2011 and his MS degree in Mechanical Engineering in New Jersey Institute of Technology in 2013. He is currently a PhD student at Maha Fluid Power Research Center in Purdue University. His main research interests are modeling and optimizing of hydraulic pumps/motors.

M. Ivantysynova was born on 11 December 1955 in Polenz (Germany). She received her MSc degree in Mechanical Engineering and her PhD degree in Fluid Power from the Slovak Technical University of Bratislava, Czechoslovakia. After 7 years in fluid power industry, she returned to university. In April 1996, she received a professorship in fluid power & control at the University of Duisburg (Germany). From 1999 until August 2004, she was a professor of Mechatronic Systems at the Technical University of Hamburg-Harburg. Since August 2004, she is a professor at Purdue University, USA. Her main research areas are energy saving actuator technology and model-based optimization of displacement machines as well as modeling, simulation, and testing of fluid power systems. Besides the book 'Hydrostatic Pumps and Motors' published in German and English, she has published more than 80 papers in technical journals and at international conferences.

References

Grönberg, D., 2011. *Prediction of case temperature of axial piston pumps*. Master thesis. Chalmers University of Technology, Sweden, ISSN 1652-8557.

Olems, L., 2001. *Ein Beitrag zur Bestimmung des Temperaturverhaltens der Kolben-Zylinder-Baugruppe von Axialkolbenmaschinen in Schrägscheibenbauweise* [The temperature behavior of the piston cylinder interface of swash plate type axial piston machines]. VDI Fortschritt-Berichte. Reihe 1 No. 348. Düsseldorf: VDI. ISBN: 3-18-334801-2.

Oppermann, M., 2006. *A new approach for failure prediction in mobile hydraulic systems*. Diss. TUHH Hamburg. VDI Fortschritt-Berichte. Reihe 12 No. 665. Hamburg: VDI. ISBN: 3-18-366512-9

Pelosi, M., 2012. *An investigation on the fluid-structure interaction of piston/cylinder interface*. Thesis (PhD). Purdue University.

Pelosi, M. and Ivantysynova, M., 2012. Heat-transfer and thermal elastic deformation analysis on the piston/cylinder interface of axial piston machines. *Transaction of the ASME, journal of tribology*, 134, 1–15.

Pelosi, M. and Ivantysynova, M., 2013. The impact of axial piston machines mechanical parts constraint conditions on the thermo-elastohydrodynamic lubrication analysis of the fluid film interfaces. *International journal of fluid power*, 14 (3), 35–51.

Schenk, A. and Ivantysynova, M., 2014. A transient fluid structure interaction model for lubrication between the slipper and swashplate in axial piston machines. Proceedings of the 9th international fluid power conference (9IFK), 24–26 March, Aachen, Germany, Vol. 1, 398–409.

Witt, K., 1974. *Die Berechnung physikalischer und thermodynamischer Kennwerte von Druckflüssigkeiten, sowie die Bestimmung des Gesamtwirkungsgrades an Pumpen unter Berücksichtigung der Thermodynamik für die Druckflüssigkeit* [The determination of physical and thermodynamic parameters of the hydraulic fluid, and the determination of pump overall efficiency considering the thermodynamic behavior of the hydraulic fluid]. Thesis (PhD). TH Eindhoven.

Zecchi, M., 2013. *A novel fluid structure interaction and thermal model to predict the cylinder block/valve plate interface performance in swash plate type axial piston machines*. Thesis (PhD). Purdue University.

Zecchi, M. and Ivantysynova, M., 2013. Spherical valve plate design in axial piston machines – A novel thermo-elasto-hydrodynamic model to predict the lubricating interface performance. *The 8th international conference on fluid power transmission and control (ICFP 2013)*, 9–11 April, Hangzhou, China, 325–629.

Zecchi, M., Mehdizadeh, A. and Ivantysynova, M., 2013. A novel approach to predict the steady state temperature in ports and case of swash plate type axial piston machines. *Proceedings of the 13th Scandinavian international conference on fluid power (SICFP2013)*, 3–5 June, Linkoping, Sweden.